RSC Advances

ROYAL SOCIETY
OF CHEMISTRY

PAPER

View Article Online
View Journal | View Issue

Check for updates

Cite this: *RSC Adv.*, 2023, **13**, 22569

Improving the decorative performance of UV-curable coatings with iridescent cellulose nanocrystal film

Mengyao Chen,[ab] Haiqiao Zhang[ab] and Yan Wu*[ab]

Cellulose nanocrystals (CNC) possess remarkable mechanical properties, a high aspect ratio, a large specific surface area, and a unique nanostructure, making them a popular choice in various fields. In this study, a CNC suspension was prepared through acid hydrolysis, and subsequently, a film exhibiting iridescence and chiral nematic structure was formed on the cured UV-WA surface *via* evaporation-induced self-assembly. The mean diameter and length of CNC were determined to be 25.1–33.3 nm and 281.3–404.2 nm, respectively, through transmission electron microscope analysis. The experimental results revealed that the color of the film significantly changes with variations in the CNC suspension concentration. Notably, the formation of the iridescent film is dependent on the concentration of CNC, with concentrations between 1.2% and 2.9% being optimal, and the aspect ratio of the CNC nanoparticles being around 11.3. X-ray diffraction analysis confirmed that the CNC nanoparticles possess the same crystal structure as microcrystalline cellulose (cellulose I). Fourier transform infrared spectroscopy revealed that the C═C bond present in the liquid UV-curable coating disappeared upon UV irradiation. The performance of the CNC iridescent film, with varying thickness, was evaluated using UV-vis spectroscopy. The thermogravimetric analysis results indicate that the addition of CNC enhances the membrane's thermal stability and heat resistance. The results indicate that as the thickness of the CNC iridescent film increases, the corresponding UV-vis spectra display a redshift. The UV-WA/CNC shows potential in the field of decoration and establishing a straightforward, cost-effective, and efficient method for producing photonic materials with structural colors.

Received 24th May 2023
Accepted 18th July 2023

DOI: 10.1039/d3ra03481j

rsc.li/rsc-advances

1. Introduction

Cellulose nanocrystals (CNC) exhibit remarkable features such as biocompatibility, substantial specific surface area, as well as high Young's modulus and tensile strength.[1,2] These qualities render it a versatile material for an extensive range of applications, such as medical products,[3] transparent conductive films,[4,5] and nanomaterial-reinforced composites.[6] The preparation techniques for CNC include chemical methods, such as sulfuric acid hydrolysis and oxidation processes,[7,8] mechanical methods,[9,10] and hybrid mechanical–chemical approaches.[11,12] Acid hydrolysis has been widely used as a well-established chemical method for the production of CNC. The characteristics of CNC such as size, aspect ratio, and yield vary with different feed ratios, sulfuric acid concentration, hydrolysis temperature, and hydrolysis time.[13] Upon reaching a certain critical concentration, CNC suspension with a specific aspect ratio can self-assemble and form a chiral nematic liquid crystal phase, also known as a cholesteric liquid crystal phase.[14] This structure can be maintained even after the CNC suspension dries, leading to the self-assembly of CNC nanoparticles into iridescent films.[15,16] The phenomenon can be explained by two theories, namely Bragg reflection and birefringence.[17,18] Bragg's formula, $\lambda = nP\sin\varphi$, expresses the relationship between the wavelength of reflected light, λ, the refractive index, n, the pitch, P, and the magnitude of the incident angle, φ. The Bragg reflection theory suggests that variations in the pitch and refractive index of CNC iridescent film result in changes in the incident angle φ, thereby reflecting different wavelengths of light, including those within the visible range. This results in the manifestation of different colors in the iridescent film. Birefringence, a phenomenon that occurs when a beam of light enters an anisotropic crystal and is refracted in two different directions, is observable when light propagates through a heterogeneous body. The propagation velocity and refractive index of light vary with the direction of vibration, and this phenomenon is known as birefringence. Birefringence theory indicates that Bragg reflection is no longer applicable to wavelengths less than the pitch of the chiral structure, which is typically in the range of 400–800 nm for visible light. Additionally, thicker CNC films exhibit a more pronounced

---

[a] College of Furnishings and Industrial Design, Nanjing Forestry University, Nanjing 210037, Jiangsu, China. E-mail: wuyan@njfu.edu.cn

[b] Jiangsu Co-Innovation Center of Efficient Processing and Utilization of Forest Resources, Nanjing 210037, Jiangsu, China

birefringence effect.[19] Water-based UV-curable coatings possess characteristics such as high efficiency, a wide range of applications, energy-saving features, environmental friendliness, and cost-effectiveness, as documented in previous studies.[20,21] The UV curing technology also shares similar features,[22,23] which are considered essential for the new green industry in the 21st century, and thus designated as the "5E" industrial technology by the International Radiation Association.[16,24] However, the decorative performance of these coatings is limited and cannot satisfy the demand for a wider range of colors.[25] To address this issue, various studies have explored the potential of using CNC to improve the performance of transparent wood coatings and water-based varnish formulations.[26,27] Despite these efforts, the currently available color options remain insufficient, and there is still a need for further improvements in the decorative performance of these coatings.[28] In recent years, architects and designers have shown interest in using special effects pigments in wood paints for furniture or floors to enhance the visual appeal of wood surfaces.[29,30] These special effects paints can create a silky finish that traditional paints cannot achieve.

In this study, we introduce a novel approach to enhance the decorative properties of UV-curable waterborne acrylate (UV-WA) by using CNC film with iridescent color.[21,31] The CNC suspension was prepared through acid hydrolysis and deposited onto the cured UV-WA surface to form an iridescent film with a chiral nematic structure that was evaporation-induced self-assemble.[32,33] The resulting film demonstrated improved hardness and more diverse colors. To evaluate the iridescence of the film, we utilized a circular dichroism spectrometer to measure both iridescent brightness and reflection.[34] We believe that this iridescent film can be applied in various settings including home furnishing, interior decoration, and architecture, such as decorative boards and softened wood floors.[35,36]

2. Experimental

2.1 Materials

The materials utilized in this research study included microcrystalline cellulose (MCC, 50 μm) obtained from Sinopharm Chemical Reagent Co., Ltd. of China, and sulfuric acid (AR, 98 wt%) procured from Nanjing Chemical Reagent Co., Ltd. (Nanjing, China). Additionally, the ultra-pure water utilized in this study was generated by a Plus-E3-10th ultra-pure water machine (EPED, China). The UV-WA coating employed in the study was obtained from Jiangsu Haitian Co., Ltd. of China. All materials were utilized as received without any further purification.

2.2 Prepared CNC suspension

The present study utilized a method for preparing CNC suspension that was previously reported in our literature.[37] The process involved a feed ratio of 200.0 g of 64 wt% H_2SO_4 and 20.0 g of MCC. The hydrolysis step was carried out at a temperature of 45 °C for 60 min. This was followed by a sequence of treatments including deacidification, dialysis, and ultrasonic treatment (Q700, QSonica, Newtown, USA). The resulting CNC suspension had a final concentration of 1.2 wt%.

2.3 Prepared UV-WA/CNC iridescent film

2.3.1 Curing of UV-WA coating. A straightforward spin-coating system was established by placing 2.0 g of UV-WA into a 60 mm plastic Petri dish. Initially, the rotational speed of the coating platform was set to 500 rpm, enabling the bottom of the Petri dish to be coated with UV-WA. Subsequently, the rotational speed was increased to 1000 rpm, causing the UV-WA to adhere to the side walls of the plastic Petri dish. This method provides a practical approach for uniformly coating substrates with UV-WA.

The plastic Petri dish coated with UV-WA should be subjected to positive radiation curing for 2 min. Subsequently, the dish should be inverted for radiation curing at the bottom for 30 s. These parameters have been previously reported in the literature.

2.3.2 Preparation of CNC iridescent decorative layer. In this study, surface modification of CNC on UV-WA coating film was investigated by drying CNC suspensions on the surface of cured UV-WA film. The experimental procedure involves removing the UV-WA film from the plastic Petri dish and applying various volumes of CNC suspensions onto the film surface. The specimens were subsequently placed in an oven at a temperature of 50 °C, and five different groups were examined. We aimed to achieve CNC iridescent films with varying thicknesses using different volumes of CNC suspensions and evaluate the differences in the decorative modification of CNC iridescent films on UV-WA coating films.

2.4 Characterization

2.4.1 Chemical structure and composition. In this study, Fourier transform infrared spectroscopy (FTIR) at attenuated total reflection (ATR) mode was employed to analyze the chemical structures and compositions of the liquid and cured UV-WA coating as well as the UV-WA/CNC. The FTIR-ATR spectra were obtained using a Vertex 80 Infrared Spectrometer manufactured by Bruker in Germany, which has a wavenumber range of 4000 cm^{-1} to 400 cm^{-1} and a resolution of 0.5 cm^{-1}. The analysis of these spectra allowed for a detailed characterization of the molecular composition of the aforementioned materials.

The X-ray diffraction (XRD) patterns for both MCC and CNC were obtained using an Ultima IV X-ray diffractometer (Rigaku, Japan) with CNC powders that were oven-dried. The diffraction XRD spectra were scanned at a rate of 5° (2θ) min^{-1} within the range of 5° and 50° (2θ). The determination of the crystal structures for both MCC and CNC was based on the XRD patterns. All XRD patterns for MCC and CNC were analyzed using MDI Jade 6.5.

2.4.2 Microscopy investigation. The present study employed transmission electron microscopy (TEM, JEM-1400, JEOL, Japan) to investigate the nanoscale morphologies of CNC nanoparticles. The CNC suspension was utilized with

0.001 wt% for sample preparation and observation. The sample preparation involved placing a 300 mesh copper grid onto a filter paper, transferring a small amount of CNC suspension onto the grid, adding a staining agent, drying the sample under an infrared lamp, and subsequently placing it into a sample rack. The sample was then pushed into the sample chamber and subjected to vacuum conditions for observation. This experimental procedure ensured the high-quality characterization of the CNC nanoparticles' morphologies with excellent resolution and fidelity. The atomic Force Microscope (AFM, Dimension Edge, Bruker, Germany) was employed to investigate the micromorphology of CNC film. The CNC suspension was dropped on the silicon chip and dried on the surrounding at 40 °C. The size distribution of CNC nanoparticles was determined using a Zetasizer Nano-ZS ZEN3600 (Malvern, Worcestershire, United Kingdom) provided with a 4 mW He–Ne (633 nm) laser with 1 mL 0.005 wt% CNC suspension.

The surface and cross-sectional morphologies of the UV-WA/CNC film were examined through the utilization of field emission scanning electron microscopy (FE-SEM) equipment, manufactured by Bruker in Germany. The sample was securely placed on the sample table and subsequently coated with a thin layer of gold. The examination process was conducted in a vacuum environment, with an accelerated voltage of 3.0 kV.

The observation of texture was conducted as follows: the CNC suspension or gel of the intended concentration was transferred to a flat capillary tube and positioned under a polarizing microscope (POM, BX-41, Olympus, Japan). The purpose of this observation was to detect the emergence of either finger texture or plane texture, which is indicative of a phase transition. This technique is commonly employed in the field of materials science to evaluate the structural and phase characteristics of materials and is a valuable tool for investigating the behavior of CNC suspensions and gels.

2.4.3 Critical concentration of liquid crystal phase. A glass Petri dish with a 35 mm diameter was utilized to contain approximately 1.0 g of CNC suspension. The drying process was performed at 80 °C for 1 h while conducting two sets of parallel tests concurrently. The solid content was determined using eqn (1).

$$\text{Solid content} = \frac{m_2 - m_0}{m_1 - m_0} \times 100 \tag{1}$$

where m_0 is the mass of the empty Petri dish, m_1 is the total mass of the CNC suspension and Petri dish, and m_2 is the total mass after drying.

Based on Table 1, a total of nine sets of CNC suspensions or gels, each with varying concentrations, are planned to be established to ascertain the concentration at which the liquid crystal phase transition occurs. For those suspensions with high concentrations, they will no longer exist in a state of suspension but rather as a gel. Subsequently, the CNC suspensions or gels with different concentrations will be subjected to a drying process, aiming to achieve a rapid film formation method. To concentrate the CNC suspensions, they will be pipetted into glass test tubes and heated in a 50 °C oven. The outcome will be CNC suspensions or gels with distinct concentrations.

2.4.4 Physical and mechanical properties

Ultraviolet-visible (UV-vis) spectrum. In this study, the UV-vis spectra (reflection, absorption, and transparency) were analyzed using a Lambda 950 (PE, USA) instrument for the UV-vis spectra of the UV-WA coating film and UV-WA/CNC film. Before testing, a circular film with a diameter of approximately 40 mm was obtained by cutting the UV-WA coating film attached to CNC iridescent film using scissors. The circular film sample to be tested was secured onto the sample rack clip and its position was adjusted to ensure that the optical path passed through the center of the sample.

Water contact Angle. In this study, the water contact angle of the UV-WA coating film was assessed using a DSA100S drop-shape analyzer manufactured by KRÜSS, Germany. To conduct the experiments, small strips measuring approximately 5.0 mm in width were cut out from various locations of the sample. Subsequently, water contact angles were measured at five different locations on each strip, and the average value was calculated to obtain an accurate representation of the film's wetting behavior.

Water resistance of CNC iridescent film. In order to ascertain whether the iridescent properties of CNC film persist after exposure to water, it is imperative to conduct appropriate tests. Given that the CNC film is hydrophilic, owing to the presence of a substantial number of hydroxyl groups on its surface, it is pertinent to examine whether it retains its iridescence upon contact with water. To accomplish this, a small quantity of ultra-pure water was dispensed onto the surface of the desiccated iridescent film, and the iridescence of the film was subsequently evaluated. The film was allowed to air-dry naturally, and its iridescent characteristics were once again analyzed.

Pencil hardness. This study involves the utilization of a pencil hardness test method to assess the hardness of UV-WA coating film, following the guidelines outlined in the "GB/T 6739-2006 Paints and Varnishes Determination of Film Hardness by Pencil Test". To conduct the test, a 400 mesh sandpaper is first used to predict the hardness of the pencil lead core relative to the axial cross-section. The pencil is then cautiously fixed on the tester to ensure that the tester remains in a horizontal position and that the coating film in contact with the lead section is not damaged. The tester is then evenly pushed forward for a minimum distance of 7 mm. The surface of the tested coating film is subsequently inspected using a magnifying glass and rubber to detect the presence of scratches of more than 3.0 mm. The hardness of the coating film is based on the hardness of the highest pencil grade that does not produce scratches exceeding 3.0 mm.

Circular Dichroism (CD) spectra. The MOS-500 Circular Dichroism Spectropolarimeter (Bio-Logic, Seyssinet-Pariset, France) was utilized to conduct the measurements presented in this study. A 1.0 mm path length rectangular cell was employed for the analysis, which was positioned perpendicularly to the incident cross-polarized light. The scanning rate was set to 100 nm min^{-1}, while the step resolution and bandwidth were maintained at 0.2 and 1 nm, respectively.

Table 1 The parameters of increasing the concentration of CNC suspensions

Sample number	Original volume (mL)	Target volume (mL)	Target concentration
1(ctrl)	—	—	1.2 wt%
2	3	2.5	1.4 wt%
3		2.0	1.8 wt%
4		1.75	2.1 wt%
5		1.5	2.4 wt%
6		1.25	2.9 wt%
7		1.0	3.6 wt%
8		0.75	4.8 wt%
9		0.5	7.2 wt%

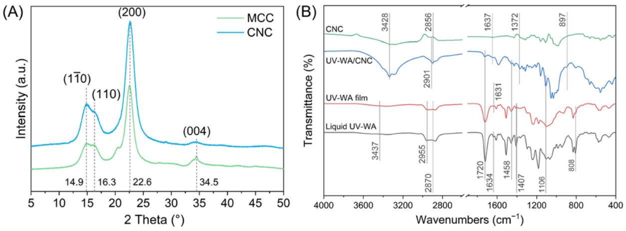

Fig. 1 (A) The XRD spectra of MCC and CNC; (B) the FTIR-ATR spectra of liquid UV-WA coating, cured UV-WA coating film, UV-WA/CNC film, and CNC film.

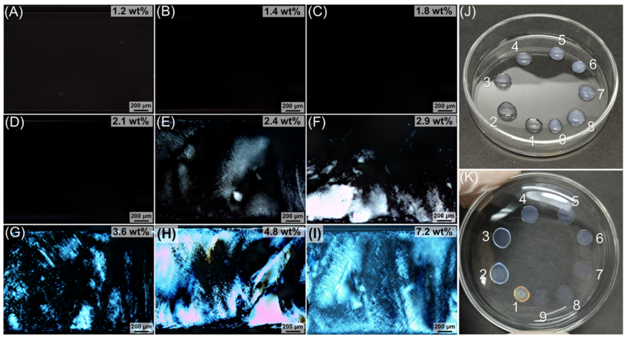

Fig. 2 (A–I) The POM images of CNC suspensions with different concentrations ranging from 1.2 wt% to 7.2 wt%; the digital images of CNC suspension with different concentrations; (J) before and (K) after drying.

Thermogravimetric analysis (TGA). The thermal behaviors of the films were analyzed by a TG 209F1 Libra thermogravimetric analyzer (Necchi, Germany). The analysis was performed at an N_2 flow rate of 50 mL min^{-1}, from 30 °C to 700 °C, and a heating rate of 10 °C min^{-1}. The power of about 5 mg for each cured film was used for measurement.

3. Results and discussion

3.1 Chemical structure and composition

Fig. 1A displays a comparative analysis of the XRD patterns between MCC and CNC. The XRD patterns exhibit typical diffraction peaks, with corresponding 2θ values of 14.9°, 16.3°, 22.6°, and 34.5°, which correspond to the (1 $\bar{1}$0), (110), (200), and (004) lattice planes of MCC and CNC, respectively. These results are consistent with previous studies.[38] Notably, the peak positions of CNC are identical to those of MCC, indicating that the crystalline structure of CNC remains unchanged, and it belongs to cellulose I.[39]

The FTIR spectra (Fig. 1B) were utilized to analyze the chemical structure of liquid UV-WA coatings and cured coating films. The disappearance of the characteristic peaks of C═C vibrations at 1634, 1407, and 808 cm^{-1} after UV irradiation suggests that the radicals reacted with C═C bonds in the liquid UV-WA coating.[40] The appearance of a new absorption peak at 1631 cm^{-1}, and the shift of the peak of C═C vibrations from 1634 cm^{-1} to 1631 cm^{-1} after UV irradiation was caused by the residual moisture present in the cured coating films. The O–H vibrations of the residual moisture can be attributed to the absorption bands at 3437 and 1631 cm^{-1}.[41] The assigned molecular vibrations for specific peaks observed in the spectroscopic analysis can be summarized as follows. The peaks located at 2955 cm^{-1} and 2870 cm^{-1} are indicative of the C–H stretching vibration occurring in CH_2 and CH_3 groups. Likewise, the peak observed at 1458 cm^{-1} corresponds to the C–H deformation vibration in CH_2 and CH_3 groups.[42] Furthermore, the absorption bands appearing around 1720 cm^{-1} and 1106 cm^{-1} can be attributed to the vibrations associated with –C═O and C–O–C, respectively.

Fig. 1B displays the FTIR spectra of CNC. The spectra reveal the O–H stretching vibration peak at 3428 cm^{-1}, as well as the

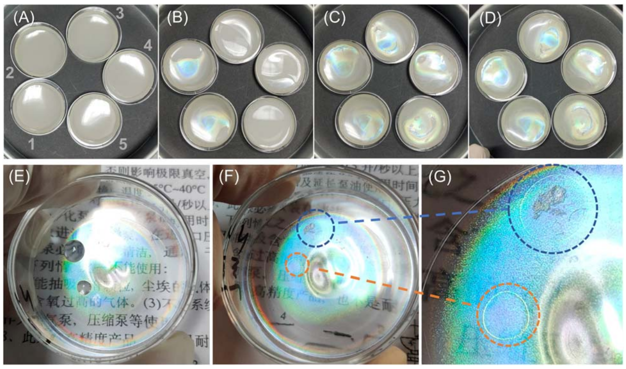

Fig. 3 The dryness process of CNC suspension of (A) as preparation, (B) after 0.25 h, (C) after 3.7 h, and (D) after 4.5 h; (E) CNC iridescent film with water droplets; (F and G) changes in the iridescent film due to artificial removal and natural evaporation of water droplets.

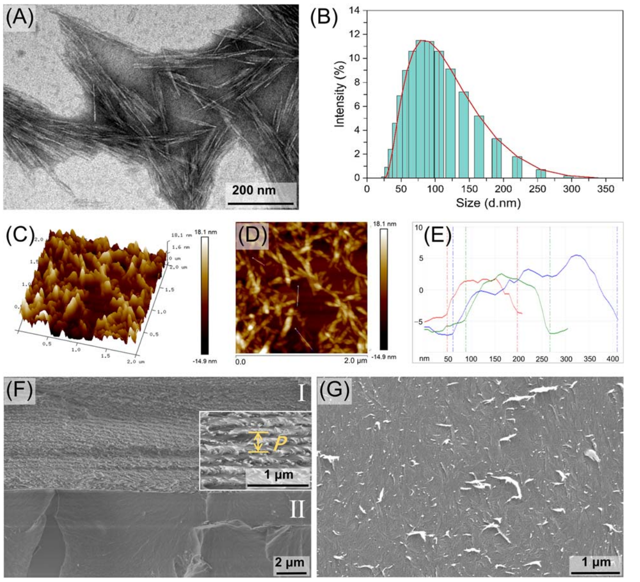

Fig. 4 (A) TEM image of CNC nanoparticles; (B) the size distribution of CNC nanoparticles; (C) 3D and (D) 2D AFM images of CNC film; (E) the profile of CNC nanoparticles based on 2D AFM image; (F) the cross-sectional FE-SEM image of UV-WA/CNC film (part I: CNC film, inset: high magnification FE-SEM image of CNC film, $P = 331.6 \pm 10.5$ nm; part II: UV-WA film); (G) the surface FE-SEM image of UV-WA/CNC film.

peak at 1372 cm^{-1} representing the O–H bending vibration. Additionally, multiple vibration peaks occur at 2901 cm^{-1}, 2856 cm^{-1}, and 897 cm^{-1}, corresponding to the symmetric and antisymmetric stretching vibrations and the deformation vibrations of C–H in cellulose.[43] Despite efforts to remove adsorbed water in CNC, the strong hydrogen bonding between the –OH of CNC and –OH of water made complete removal difficult. As a result, a peak near 1637 cm^{-1} attributed to the O–H bending vibration of the remaining water in CNC was present. The FTIR-ATR spectra indicated that UV-WA/CNC detected functional groups of both the CNC film on the surface and the coating film below, as evidenced by the peak value near 1722 cm^{-1}, which was absent in CNC alone. This peak was attributed to the C=O group in the coating film.

3.2 Analysis of critical concentration of liquid crystal phase of CNC suspension

The results of the present study demonstrate the POM observations of nine groups of CNC suspensions with varying concentrations, as depicted in Fig. 2. As depicted in Fig. 2A–D, the POM images of CNC suspensions with concentrations ranging from 1.2 wt% to 2.1 wt% did not exhibit any distinct planar texture, indicating isotropy within this concentration range. However, in Fig. 2E–I, the planar texture was observed in the visual field of CNC suspensions with a concentration of 2.4 wt%, suggesting the emergence of the liquid crystal phase of CNC suspension. Furthermore, the critical concentration of transition was approximately 2.4 wt%, which was consistent with previous literature reports.[44]

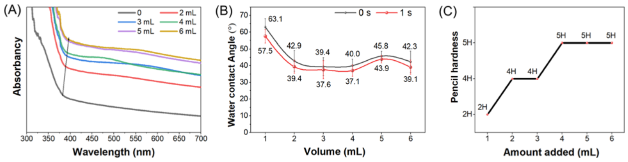

Fig. 5 (A) UV-vis absorption spectra, (B) water contact angles, and (C) pencil hardness of UV-WA/CNC films.

Fig. 2J depicts the varying concentrations of CNC suspension, which range from 1.2 wt% to 7.2 wt%. Specifically, the concentrations are 1.2 wt%, 1.4 wt%, 1.8 wt%, 2.1 wt%, 2.4 wt%, 2.9 wt%, 3.6 wt%, 4.8 wt%, and 7.2 wt%, respectively. It is observed that the color of the suspension transitions from colorless and transparent to light blue and translucent as the concentration increases. Meanwhile, Fig. 2K illustrates the dried CNC suspensions with different concentrations after being subjected to an oven at 80 °C. The original CNC suspension had a golden yellow color when dried, but the color of the resulting film changed from blue to colorless as the concentration increased. However, CNC suspensions with concentrations of 3.6 wt%, 4.8 wt%, and 7.2 wt% did not form iridescent films and only left partial traces after drying. Consequently, the experimental approach of forming an iridescent film by thickening the CNC suspension before drying to expedite the drying process could not be realized.

3.3 Macro characteristics of UV-WA/CNC iridescent film

During the evaporation-induced self-assembly process, the formation of an iridescent film was repeatedly observed and recorded through photography. The drying process of suspensions containing CNC was monitored in Petri dishes 1-5, which contained 2 mL, 3 mL, 4 mL, 5 mL, and 6 mL of CNC suspensions, respectively, as illustrated in Fig. 3A–D. The iridescent film displayed hydrophilic characteristics, which can be attributed to the hydroxyl group's hydrophilic nature on the CNC surface, as depicted in Fig. 3E–G. Following the evaporation of water, the iridescent properties reappeared, and a boundary emerged, corresponding to the edge of the original droplet. This boundary is known as the coffee ring phenomenon, which is associated with the droplet's profile height during the drying process. The outcomes suggest that the CNC iridescent film is not water-resistant; nonetheless, it still retains the iridescent properties after being dried again.

Based on the information presented in Fig. 3E, it is evident that the iridescence film exhibited notable hydrophilic characteristics, resulting in the swift disappearance of iridescence in the water-stained region. This phenomenon is attributed to the hydroxyl group's hydrophilicity on the surface of the CNC.[45] Moreover, as illustrated in Fig. 3G, the removal of water droplets during the re-evaporation process caused a disruption in the original structure and led to the disappearance of iridescence, indicated by the blue circle. However, after the water had dried, the iridescence characteristic reappeared in the orange circle, and a boundary corresponding to the original droplet's edge emerged, which is known as the coffee ring effect. This effect is

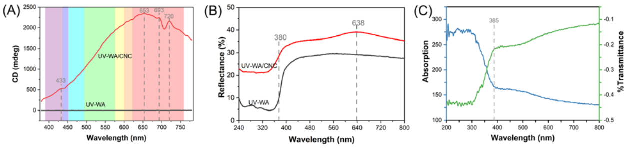

Fig. 6 (A) The CD spectra of UV-WA and UV-WA/CNC; (B) the UV-vis reflectance spectra of UV-WA and UV-WA/CNC; (C) the absorption and transmittance spectra of UV-WA/CNC.

linked to the droplet's profile height during drying.[46] The findings suggest that although the CNC iridescence film is not water-resistant, it can still exhibit iridescence features after drying again.

3.4 Morphology of CNC and UV-WA/CNC

Fig. 4 depicts the microstructure of CNC examined in the present study. The CNCs acquired in this investigation exhibited a rod-like shape with both their length and diameter measuring in the nanoscale range, which is consistent with the literature findings.[47] Recent research has emphasized the criticality of the aspect ratio of rod-shaped CNCs in producing iridescent films during suspension drying.[48,49] In particular, when the aspect ratio of CNC is either too small or too large, the color complexity of the CNC suspension-derived film after drying is reduced.[14] Notably, the aspect ratio of the CNCs prepared in this study was around 11.3, providing a crucial foundation for their iridescence upon drying.

The TEM image and size distribution of CNC nanoparticles are shown in Fig. 4A and B. The average size of CNC nanoparticles is 79.9 nm, and the maximum mean Intensity is 11.5%. Fig. 4C and D show the 3D and 2D AFM images of CNC film, respectively. The profile of CNC nanoparticles based on a 2D AFM image is shown in Fig. 4E, the results are consistent with the TEM image results, but different from the particle size analysis, because the particle size analysis test is the result of simulated particle size, not the true size of CNC. The FE-SEM images presented in Fig. 4F depict the microscopic morphology of a CNC iridescent film on the UV-WA surface. Specifically, Fig. 4F illustrates the cross-sectional view of CNC iridescent film on the UV-WA surface, revealing a layered structure resulting from the chiral spiral self-assembly process. The orderly arrangement of the film's surface further exemplifies its intricate structure. The UV-WA coating exhibits a pronounced interaction with CNC, as depicted in Fig. 1B, where carboxyl groups are present on the coating film and hydroxyl groups are present on the CNC. The compatibility between these functional groups facilitates the formation of robust hydrogen bonds. The SEM images reveal a tight and void-free adhesion between the coating and the CNC, further confirming the strength of their interaction. Fig. 4G displays the FE-SEM image CNC iridescent film's surface. The CNC nanoparticles on FE-SEM showed a locally ordered arrangement, and the particle size was consistent with the TEM image.

Additionally, as observed through the FE-SEM images, the thickness of the film produced following the drying of varying amounts of CNC suspension was found to be non-uniform. The thickness of the film is a significant factor affecting the smoothness and levelness of the UV-WA film upon drying. Hence, the approximate thickness of the CNC film can be ascertained through FE-SEM examination. In this study, the mean values of various test locations were computed to obtain the groups of CNC suspension of 2 mL, 3 mL, 4 mL, 5 mL, and 6 mL. The thicknesses of the resulting films upon drying were determined as 21.3 μm, 32.8 μm, 38.3 μm, 45.1 μm, and 69.6 μm, respectively.

3.5 Analysis of physical and mechanical properties

Based on previous research,[50] the UV-vis absorption spectrum of CNC iridescent film is subject to numerous factors, and the resulting UV-vis spectrum is directly linked to the color of the CNC iridescent film.[51] This investigation aimed to evaluate the UV-vis performance of CNC iridescent film with varying thicknesses. The observed trend demonstrated a redshift phenomenon in the corresponding UV-vis spectrum as the thickness of the CNC iridescent film increased, as shown in Fig. 5A. The naked eye was able to perceive changes in the film's appearance with increased thickness. When the original volume of CNC suspension was 3 mL or 4 mL, the resulting UV-vis spectra of the dried films were comparable, as were the cases when the volume of the original CNC suspension was 5 mL or 6 mL. This is attributed to the uneven deposition of the CNC suspension on the coating film's surface, resulting in uneven film thickness. The flattest region was selected for UV-vis spectrum testing in this experiment.

Fig. 5B presents the experimental findings for the water contact angle of UV-WA coated surfaces, demonstrating both the angle of the water droplets upon initial contact with CNC iridescence film and the water contact angle after 1 s. Results indicate that the water contact angle of the UV-WA/CNC film was notably lower than that of the UV-WA coating film. Specifically, the maximum and minimum contact angles observed for CNC iridescent film were 45.8° and 39.4°, respectively, representing a 17.3° and 23.7° decrease compared to the UV-WA coating film. After 1 s of contact, the water contact angle of the UV-WA/CNC film was measured at 57.5°. The results

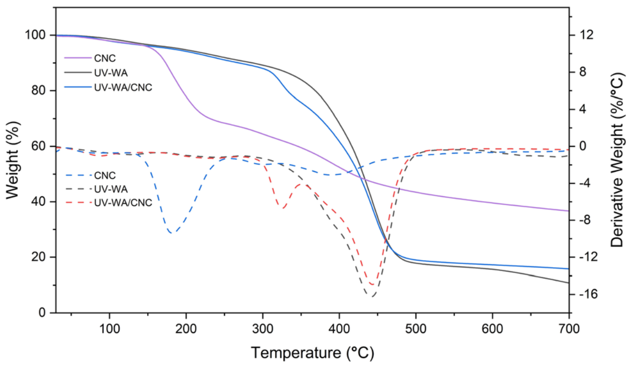

Fig. 7 The thermal properties of the cured UV-WA coating film, UV-WA/CNC film, and CNC film.

Table 2 Pyrolysis parameters of UV-WA, UV-WA/CNC, and CNC films

Film	$T_{5\%}$ (°C)	$T_{50\%}$ (°C)	1st deg. stage		2nd deg. stage		Residue (%)
			$T_{\max}$ (°C)	$\mathrm{DTG}_{\max}$ (%/°C)	$T_{\max}$ (°C)	$\mathrm{DTG}_{\max}$ (%/°C)	
UV-WA	196.6	430.6	—	—	439.6	16.16	10.91
CNC	157.6	413.6	180.56	9.38	388.6	3.08	36.71
UV-WA/CNC	191.6	420.4	323.6	6.66	440.6	14.81	15.82

demonstrate that CNC iridescent film as a surface modification material for UV-WA paint can significantly reduce the water contact angle. This decrease in contact angle is primarily attributed to the hydrophilic hydroxyl group present on the surface of CNC. By attaching a layer of CNC film onto the modified UV-WA coating film surface, the water contact angle is significantly altered. The outcome of this study is consistent with the established fact that the chemical composition and surface roughness of the solid are key factors influencing the water contact angle.[52]

Fig. 5C displays the outcomes of the pencil hardness test performed on the UV-WA coating film. The unaltered UV-WA coating exhibits a pencil hardness of 2H, while the UV-WA/CNC film demonstrates a pencil hardness of 4H after being dried with CNC suspensions of 2 mL and 3 mL. Furthermore, the UV-WA/CNC film coating shows a pencil hardness of 5H when dried with CNC suspensions of 4 mL, 5 mL, and 6 mL. This finding signifies that the surface modification hardness of the CNC iridescent film surpasses expectations. Pencil hardness is an advantageous method for evaluating the hardness of a film surface,[53] as it allows for accurate testing. During the examination, the hardness of the substrate is closely related to that of the surface film. The test outcomes of this study demonstrated that the pencil hardness reached 5H, which exceeded expectations, and was attributed to the hardening of the UV-WA coating film during the drying process of the CNC suspension at 50 °C.

3.6 Characterization of films by circular dichroism

The optical characteristics of CNC films arise from their chiral nematic structure, which reflects circularly polarized light. As demonstrated in Fig. 6A, the presence of three distinct peaks at wavelengths of 653, 693, and 720 nm results in a red appearance. Additionally, the films exhibit a peak at 435 nm, corresponding to the color purple. Notably, Fig. 6B demonstrates that the CNC films possess superior decorative properties as they transmit visible light above 380 nm.[54] The presence of a peak at 638 nm indicates a red hue, which corresponds to the peak at 653 nm observed in the CD diagram. Based on the data presented in Fig. 6C, it is evident that a conspicuous absorption peak prominently emerges at a wavelength of 385 nm, which illustrates that the CNC films possess commendable aesthetic attributes, as they exhibit high transmittance of visible light beyond the 385 nm threshold.

3.7 Thermal stability

The thermal properties of the cured UV-WA coating film, UV-WA/CNC film, and CNC film were examined through TGA and derivative weight loss (DTG) curves, as depicted in Fig. 7. Supplementary data were recorded in Table 2 to further investigate the degradation characteristics of these films. This included the temperatures at which 5% and 10% mass loss occurred (referred to as $T_{5\%}$ and $T_{10\%}$, respectively), the percentage of residual mass at 700 °C, and the maximum rate of weight loss and the corresponding temperature during the degradation stage.

The experimental findings indicate that UV-WA exhibits a weight loss phase that resembles a characteristic peak at approximately 440 °C. Within the temperature range of 291 °C to 522 °C, a weight loss of 72% was observed. At 700 °C, the residual mass percentages for UV-WA, UV-WA/CNC, and CNC films were determined as 10.91%, 15.82%, and 36.71%, respectively. These results indicate that CNC demonstrates the highest level of thermal stability, while the UV-WA/CNC film exhibits slightly greater thermal stability compared to the UV-WA film alone. Therefore, the incorporation of CNC in UV-WA films is shown to enhance their thermal stability and heat resistance.

4. Conclusions

CNC is a renewable material with high potential in many applications. Due to its unique self-assembly and optical properties, CNC tends to behave as an iridescent pigment. The innovation of this experiment lies in the excellent decorative performance of CNC coated on the coating surface. It provides an excellent application prospect for pulp and paper, which is a renewable resource. The decorative performance of UV-WA coating film is limited, thus failing to satisfy the demand for richer colors. To address this issue, CNC iridescent film is employed in this study to modify the UV-WA coating film. The resulting UV-vis spectrum exhibits a red shift phenomenon, which becomes more prominent with an increased thickness of CNC film. The CNC suspension used in the study was prepared *via* acid hydrolysis, yielding a CNC suspension concentration of 1.2 wt%, with a liquid crystal phase transition concentration of 2.4 wt%. The CNC iridescent film possesses pronounced hydrophilicity, and upon evaporation of the water on its surface, the iridescent characteristics are restored, leaving behind a boundary position of water droplets. Compared to unmodified UV-WA film, the water contact angle of UV-WA/CNC film is smaller, yet its pencil hardness improves by 3 grades, from 2H to 5H, indicating an enhancement in mechanical properties. The color of the UV-WA/CNC film surface was characterized using a circular dichroism spectrometer, which revealed that the iridescent film possesses a range of wavelengths of visible light, thereby demonstrating its exceptional decorative properties. This modified film has potential applications in various settings, such as interior decoration, architecture, and decorative boards, including softened wood floors.

Author contributions

Mengyao Chen: conceptualization, data curation, investigation, writing – original draft, writing – review & editing. Haiqiao Zhang: investigation, writing – review & editing. Yan Wu: methodology, conceptualization, supervision. All authors have read and approved the manuscript for publication.

Conflicts of interest

The authors declare that they have no known competing financial interests or personal relationships that could have appeared to influence the work reported in this paper.

Acknowledgements

The authors gratefully acknowledge the financial support from the National Natural Science Foundation of China (32071687 and 32001382) and the Postgraduate Research & Practice Innovation Program of Jiangsu Province (No. KYCX23_1197).

References

1 A. Sturcova, G. R. Davies and S. J. Eichhorn, Elastic modulus and stress-transfer properties of tunicate cellulose whiskers, *Biomacromolecules*, 2005, **2**(6), 1055–1061.

2 S. Iwamoto, W. H. Kai, A. Isogai and T. Iwata, Elastic Modulus of Single Cellulose Microfibrils from Tunicate Measured by Atomic Force Microscopy, *Biomacromolecules*, 2009, **9**(10), 2571–2576.

3 W. Czaja, A. Krystynowicz, S. Bielecki and R. M. Brown, Microbial cellulose - the natural power to heal wounds, *Biomaterials*, 2006, **2**(27), 145–151.

4 X. X. Yan, L. Wang and X. Y. Qian, Effect of High-Temperature Calcined Wheat Straw Powder after Lignin Removal on Properties of Waterborne Wood Coatings, *Coatings*, 2019, **7**(9), 444.

5 L. Valentini, S. B. Bon, E. Fortunati and J. M. Kenny, Preparation of transparent and conductive cellulose nanocrystals/graphene nanoplatelets films, *J. Mater. Sci.*, 2014, **3**(49), 1009–1013.

6 F. Yang, Y. Wu, S. Q. Zhang, H. M. Zhang, S. L. Zhao, J. L. Zhang and B. H. Fei, Mechanical and Thermal Properties of Waterborne Polyurethane Coating Modified through One-Step Cellulose Nanocrystals/Graphene Materials Sols Method, *Coatings*, 2020, **1**(10), 40.

7 H. Kargarzadeh, I. Ahmad, I. Abdullah, A. Dufresne, S. Y. Zainudin and R. M. Sheltami, Effects of hydrolysis conditions on the morphology, crystallinity, and thermal stability of cellulose nanocrystals extracted from kenaf bast fibers, *Cellulose*, 2012, **3**(19), 855–866.

8 Z. Man, N. Muhammad, A. Sarwono, M. A. Bustam, M. V. Kumar and S. Rafiq, Preparation of Cellulose Nanocrystals Using an Ionic Liquid, *J. Polym. Environ.*, 2011, 3(19), 726–731.

9 Y. Jiang, X. Y. Liu, Q. Yang, X. P. Song, C. R. Qin, S. F. Wang and K. C. Li, Effects of residual lignin on composition, structure and properties of mechanically defibrillated cellulose fibrils and films, *Cellulose*, 2019, **3**(26), 1577–1593.

10 J. H. Li, X. Y. Wei, Q. H. Wang, J. C. Chen, G. Chang, L. X. Kong, J. B. Su and Y. H. Liu, Homogeneous isolation of nanocellulose from sugarcane bagasse by high pressure homogenization, *Carbohydr. Polym.*, 2012, **4**(90), 1609–1613.

11 W. L. Lim, A. A. N. Gunny, F. H. Kasim, S. C. B. Gopinath, N. H. I. Kamaludin and D. Arbain, Cellulose nanocrystals from bleached rice straw pulp: acidic deep eutectic solvent versus sulphuric acid hydrolyses, *Cellulose*, 2021, **10**(28), 6183–6199.

12 J. A. Sirvio, M. Visanko and H. Liimatainen, Deep eutectic solvent system based on choline chloride-urea as a pre-treatment for nanofibrillation of wood cellulose, *Green Chem.*, 2015, **6**(17), 3401–3406.

13 M. M. Mahmud, A. Perveen, R. A. Jahan, M. A. Matin, S. Y. Wong, X. Li and M. T. Arafat, Preparation of different polymorphs of cellulose from different acid hydrolysis medium, *Int. J. Biol. Macromol.*, 2019, **130**, 969–976.

14 G. M. Zhao, S. Zhang, S. C. Zhai and M. Z. Pan, Fabrication and characterization of photonic cellulose nanocrystal films with structural colors covering full visible light, *J. Mater. Sci.*, 2020, **20**(55), 8756–8767.

15 X. X. Yan, W. T. Zhao and L. Wang, Preparation and Performance of Thermochromic and Self-Repairing Dual Function Coating film with Lac Resin Microcapsules and Fluorane Microcapsules, *Polymers*, 2021, **18**(13), 3109.

16 X. X. Yan, W. B. Li, Y. Han and T. Y. Yin, Preparation of Melamine/Rice Husk Powder Coated Shellac Microcapsules and Effect of Different Rice Husk Powder Content in Wall Material on Properties of Wood Waterborne Primer, *Polymers*, 2022, **1**(14), 72.

17 Y. Su, B. F. Zhang, Y. Zhu and Y. Q. Li, Sensing circular birefringence by polarization-dependent parameters in fiber Bragg gratings and the influence of linear birefringence, *Opt. Fiber Technol.*, 2012, **1**(18), 51–57.

18 O. R. Juarez-Rivera, R. A. Mauricio-Sanchez, K. Jarrendahl, H. Arwin and A. Mendoza-Galvan, Shear-Coated Linear Birefringent and Chiral Cellulose Nanocrystal Films Prepared from Non-Sonicated Suspensions with Different Storage Time, *Nanomaterials*, 2021, **9**(11), 2239.

19 S. Y. Cheng, K. S. Chiang and H. P. Chan, Birefringence characteristics of benzocyclobutene rib optical waveguides, *Electron. Lett.*, 2004, **6**(40), 372–374.

20 X. X. Yan, Y. Tao and X. Y. Qian, Preparation and Optimization of Waterborne Acrylic Core Microcapsules for Waterborne Wood Coatings and Comparison with Epoxy Resin Core, *Polymers*, 2020, **10**(12), 2366.

21 W. W. Peng and X. X. Yan, Preparation of Tung Oil Microcapsule and Its Effect on Wood Surface Coating, *Polymers*, 2022, **8**(14), 1536.

22 X. X. Yan and L. Wang, Preparation of Shellac Resin Microcapsules Coated with Urea Formaldehyde Resin and Properties of Waterborne Coating films for Tilia amurensis Rupr, *Membranes*, 2020, **10**(10), 278.

23 H. Q. Zhang, Y. Wu, J. L. Zhang, Z. H. Wu and X. X. Zhan, Separation cellulose nanocrystals from microcrystalline cellulose using hydrated deep eutectic solvent and high shear force, *Ind. Crops Prod.*, 2022, **189**, 115781.

24 X. X. Yan, Y. Han and T. Y. Yin, Synthesis of Urea-Formaldehyde Microcapsule Containing Fluororesin and Its Effect on Performances of Waterborne Coatings on Wood Surface, *Polymers*, 2021, **11**(13), 1674.

25 M. S. Vlad-Cristea, V. Landry, P. Blanchet and C. Ouellet-Plamondon, Nanocrystalline Cellulose as Effect Pigment in Clear Coatings for Wood, *ISRN Nanomater.*, 2013, **2013**, 1–12.

26 A. Kaboorani, N. Auclair, B. Riedl, O. Hosseinaei and S. Q. Wang, Cellulose nanocrystal (CNC)-based nanocomposites for UV curable high-solid coating systems, *J. Coat. Technol. Res.*, 2017, **5**(14), 1137–1145.

27 F. Gruneberger, T. Kunniger, T. Zimmermann and M. Arnold, Rheology of nanofibrillated cellulose/acrylate systems for coating applications, *Cellulose*, 2014, **3**(21), 1313–1326.

28 X. Q. Xiong, Q. R. Ma, Y. Y. Yuan, Z. H. Wu and M. Zhang, Current situation and key manufacturing considerations of green furniture in China: a review, *J. Clean. Prod.*, 2020, **267**, 121957.

29 M. Bibu and F. Ciofu, Metallographical Aspects of the Application of Special Paint Layers for the Protection of Machine Part Sections against the Effect of lonitriding, MATEC Web of Conferences, *EDP Sci.*, 2019, **290**, 03002.

30 X. X. Yan and W. W. Peng, Preparation of Microcapsules of Urea Formaldehyde Resin Coated Waterborne Coatings and Their Effect on Properties of Wood Crackle Coating, *Coatings*, 2020, **8**(10), 764.

31 X. X. Yan and Y. J. Chang, Investigation of the Properties of Color-Changing Powder Water-Based Coating, *Coatings*, 2020, **9**(10), 815.

32 B. A. Umanskii and I. V. Simdyankin, Circular Dichroism in Cholesteric Liquid Crystals, *Crystallogr. Rep.*, 2019, **3**(64), 437–442.

33 X. X. Yan, L. Wang and X. Y. Qian, Effect of Urea-Formaldehyde-Coated Epoxy Microcapsule Modification on Gloss, Toughness and Chromatic Distortion of Acrylic Copolymers Waterborne Coating, *Coatings*, 2019, **4**(9), 239.

34 Y. Q. Qi, L. M. Shen, J. L. Zhang, J. Yao, R. Lu and T. Miyakoshi, Species and release characteristics of VOCs in furniture coating process, *Environ. Pollut.*, 2019, **245**, 810–819.

35 Y. Tao and X. X. Yan, Influence of HLB Value of Emulsifier on the Properties of Microcapsules and Self-Healing Properties of Waterborne Coatings, *Polymers*, 2022, **7**(14), 1304.

36 H. Q. Zhang, Y. Wu, F. Yang, H. L. Dong, Y. Q. Bian, H. L. Jia, X. Q. Xie and J. L. Zhang, Using Cellulose Nanocrystal as Adjuvant to Improve the Dispersion Ability of Multilayer Graphene in Aqueous Suspension, *Front. Bioeng. Biotechnol.*, 2021, **9**, 638744.

37 X. X. Yan, Y. J. Chang and X. Y. Qian, Effect of the Concentration of Pigment Slurry on the Film Performances of Waterborne Wood Coatings, *Coatings*, 2019, **10**(9), 635.

38 Y. D. He, Z. L. Zhang, J. Xue, X. H. Wang, F. Song, X. L. Wang, L. L. Zhu and Y. Z. Wang, Biomimetic Optical Cellulose Nanocrystal Films with Controllable Iridescent Color and Environmental Stimuli-Responsive Chromism, *ACS Appl. Mater. Interfaces*, 2018, **6**(10), 5805–5811.

39 Y. Z. Liu, B. T. Guo, Q. Q. Xia, J. Meng, W. S. Chen, S. X. Liu, Q. W. Wang, Y. X. Liu, J. Li and H. P. Yu, Efficient Cleavage of Strong Hydrogen Bonds in Cotton by Deep Eutectic Solvents and Facile Fabrication of Cellulose Nanocrystals in High Yields, *ACS Sustain. Chem. Eng.*, 2017, **9**(5), 7623–7631.

40 F. Bauer, R. Flyunt, K. Czihal, H. Langguth, R. Mehmert, R. S. Chubert and M. R. Buchmeiser, UV curing and matting of acrylate coatings reinforced by nano-silica and micro-corundum particles, *Prog. Org. Coat.*, 2007, **2**(60), 121–126.

41 Z. Y. Yang, J. B. Wu, G. Z. Ma, C. Y. Hou, Y. X. Niu, H. F. Duan and X. G. Hao, Effect of the particle sizes of silica on the properties of UV-curing matting coatings, *J. Coat. Technol. Res.*, 2021, **1**(18), 183–192.

42 Q. W. Yong, F. W. Nian, B. Liao, L. P. Huang, L. Wang and H. Pang, Synthesis and characterization of solvent-free waterborne polyurethane dispersion with both sulfonic and carboxylic hydrophilic chain-extending agents for matt coating applications, *RSC Adv.*, 2015, **130**(5), 107413–107420.

43 H. L. Dong, M. Li, Y. C. Jin, Y. Wu, C. X. Huang and J. L. Yang, Preparation of Graphene-Like Porous Carbons With Enhanced Thermal Conductivities From Lignin Nano-particles by Combining Hydrothermal Carbonization and Pyrolysis, *Front. Energy Res.*, 2020, **8**, 148.

44 A. Gencer, C. Schutz and W. Thielemans, Influence of the Particle Concentration and Marangoni Flow on the Formation of Cellulose Nanocrystal Films, *Langmuir*, 2017, **1**(33), 228–234.

45 R. Xiong, Y. Y. Han, Y. R. Wang, W. Zhang, X. X. Zhang and C. H. Lu, Flexible, highly transparent and iridescent all-cellulose hybrid nanopaper with enhanced mechanical strength and writable surface, *Carbohydr. Polym.*, 2014, **113**, 264–271.

46 X. Y. Mu and D. G. Gray, Droplets of cellulose nanocrystal suspensions on drying give iridescent 3-D "coffee-stain" rings, *Cellulose*, 2015, **2**(22), 1103–1107.

47 C. Olivier, C. Moreau, P. Bertoncini, H. Bizot, O. Chauvet and B. Cathala, Cellulose Nanocrystal-Assisted Dispersion of Luminescent Single-Walled Carbon Nanotubes for Layer-by-Layer Assembled Hybrid Thin Films, *Langmuir*, 2012, **34**(28), 12463–12471.

48 K. W. Klockars, B. L. Tardy, M. Borghei, A. Tripathi, L. G. Greca and O. J. Rojas, Effect of Anisotropy of Cellulose Nanocrystal Suspensions on Stratification, Domain Structure Formation, and Structural Colors, *Biomacromolecules*, 2018, **7**(19), 2931–2943.

49 F. Su, D. G. Liu, M. Y. Li, Q. Li, C. Liu, L. Liu, J. He and H. H. Qiao, Mesophase transition of cellulose nanocrystals

aroused by the incorporation of two cellulose derivatives, *Carbohydr. Polym.*, 2020, **233**, 115843.

50 F. C. Nan, Q. Chen, P. Liu, S. Nagarajan, Y. X. Duan and J. M. Zhang, Iridescent graphene/cellulose nanocrystal film with water response and highly electrical conductivity, *RSC Adv.*, 2016, **96**(6), 93673–93679.

51 M. Y. Gu, C. Y. Jiang, D. G. Liu, N. Prempeh and Smalyukh II, Cellulose Nanocrystal/Poly(ethylene glycol) Composite as an Iridescent Coating on Polymer Substrates: Structure-Color and Interface Adhesion, *ACS Appl. Mater. Interfaces*, 2016, **47**(8), 32565–32573.

52 Y. J. Kim and B. K. Kim, Synthesis and properties of silanized waterborne polyurethane/graphene nanocomposites, *Colloid Polym. Sci.*, 2014, **1**(292), 51–58.

53 Y. Kim, A. Sung, Y. Seo, S. Hwang and H. Kim, Measurement of hardness and friction properties of pencil leads for quantification of pencil hardness test, *Adv. Appl. Ceram.*, 2016, **8**(115), 443–448.

54 H. Q. Zhang, J. Gan, Y. Wu and Z. H. Wu, Biomimetic high water adhesion superhydrophobic surface via UV nanoimprint lithography, *Appl. Surf. Sci.*, 2023, **633**, 157610.